# Electrical, Mechanical, and Aerodynamics Study to Implement a Hydrogen-Powered Fixed-Wing RPAS

C. Delgado, F. Segura, and J. M. Andújar, *Senior Member, IEEE*

***Abstract*— Transport sector must be adapted to new energy model and integrate solutions that allow sustainable mobility, breaking dependency on oil and decreasing greenhouse emissions. In this sense, hydrogen technology is being considered a viable and reasonable alternative fuel. Then, in aerial transport applications, key challenges like weight and autonomy restrict possible solutions. This article proposes the design and sizing from an electrical, mechanical, and aerodynamics point of view of a hydrogen-powered remotely piloted aircraft systems (RPAS). A detailed description of requirements at time that a justification of components selection is presented. Results show that it is possible to integrate hydrogen technology on aerial platforms, providing a series of advantages, such as an autonomy enhancement, emissions reduction, and low acoustic footprint.**

***Index Terms*— Aerodynamics analysis, electrical design, fixed-wing remotely piloted aircraft systems (RPAS), hydrogen-powered, mechanical study.**

## I. Introduction

THE transport sector is in a period of adaptation toward the elimination of vehicles propelled by fossil fuels, and hydrogen is being considered a viable and reasonable alternative fuel. Yearly aviation accounts for 2% of global energy-related greenhouse emissions, having grown faster in recent decades than rail, road, or shipping [1]. Then, even the efficiency of the engines used in the aviation sector has improved significantly, reducing the fuel burned per flight by 23% since 2012 until today, the number of flights has also increased by 60% [2]. Therefore, solutions based on alternative energy sources, which reduce the problems already discussed, are vital for the future of aviation. In particular, remotely piloted aircraft systems (RPAS) are attracting interest in applications requiring precision, real-time, quality of observation and actuation, hostile scenarios, and large exploration area. In this sense, this work presents the electrical design, mechanical sizing, and aerodynamic analysis to implement a hydrogen-powered, zero-emission, extended-range fixed-wing RPAS. The starting point was a gasoline-powered RPAS with a range of 60 min that was upgraded to an electric battery-powered RPAS with a range of 90 min in [8]. Now, in this new upgraded version, the authors take on the challenge of developing the hydrogen-powered version, hybridizing battery and hydrogen fuel cell (FC). Fig. 1 shows a real image of the RPAS object of this work, and Table I shows the technical characteristics of the initial RPAS propelled by gasoline. Regarding the interior space available to integrate the hydrogen propulsion system, 0.02922 $m^3$ is the maximum space available.

Regarding previous scientific literature, very few articles have been working on RPAS design from the three points of views jointly: electrical, mechanical, and aerodynamics. Then, in [3], the need to publish systematic studies to address the design of a hydrogen-powered aircraft was yet discussed. Most of recent articles are strongly focused on the design of the electrical propulsion [4], and the energy management system

Fig. 1. RPAS on the launching platform.

TABLE I
TECHNICAL CHARACTERISTICS OF THE INITIAL GASOLINE-BASED RPAS

| Characteristics | Value |
|---|---|
| Wingspan | 3.03 m |
| Length | 1.8 m |
| MTOW (Max. Take-Off Weight) | 25 kg |
| Wing Area | 0.85 $m^2$ |
| Max. Payload | 7.5 kg |
| Autonomy (cruise phase) | 60 min |
| Speeds | 50–225 km/h |
| ROC (Rate of Climb) | 6 m/s |
| Range | 50 km |

Manuscript received 29 January 2024; revised 4 June 2024; accepted 29 June 2024. Date of publication 15 July 2024; date of current version 3 February 2025. This work was supported in part by the Spanish Government under Grant PID2020-116616RB-C31 and Grant RED2022-134588-T and in part by the Universidad de Huelva/CBUA. *(Corresponding author: C. Delgado.)*

The authors are with the Research Centre on Technology, Energy and Sustainability (CITES), University of Huelva, 21004 Huelva, Spain (e-mail: cirilo.delgado@pi.uhu.es).

Digital Object Identifier 10.1109/TTE.2024.3427015

TABLE II
ENERGY REQUIREMENTS FOR STANDARD FLIGHT

| Phase | $V_0$ (m/s) | $V_f$ (m/s) | λ (°) | t (min) | Max. Power (kW) | Energy (J) |
|---|---|---|---|---|---|---|
| Ascent 1 | 15 | 32 | 10 | 0.6 | 3.9 | $1.4 \cdot 10^5$ |
| Ascent 2 | 32 | 32 | 10 | 1.8 | 2.7 | $2.9 \cdot 10^5$ |
| Cruise | 32 | 32 | 0 | 82.9 | 0.54 | $2.6 \cdot 10^6$ |
| Descent | 32 | 0 | 2.54 | 4.7 | 0 | 0 |
| TOTAL | - | - | - | 90 | - | $3.34 \cdot 10^6$ |

*$V_0$: initial launching speed, $V_f$: final speed, λ: launching angle

to guarantee the electrical propulsion power [5]. By contrast, research works including mechanical sizing and aerodynamics analysis of the performance of the aerial platform are really scarce [6], [7].

Based on above, the main contributions of this article are listed below.

1) The article presents the design of the hydrogen technology-based propulsion system for a fixed-wing RPAS.
2) The propulsion system is electrically powered by a FC. The propulsion system is tested from the point of view of endurance and autonomy.
3) The FC is home-designed, due to no commercial FC has been found that can be integrated inside the aerial platform.
4) The research includes a mechanical study to integrate the designed propulsion system inside the aerial platform: components sizing, space occupancy, and calculation of the gravity center.
5) The last contribution is the aerodynamics analysis. The work includes a study of air intakes over the aircraft. The results demonstrate both aircraft stability and air intake are guaranteed.

## II. HYDROGEN-POWERED FIXED-WING RPAS—BACKGROUND AND PREVIOUS REQUIREMENTS

The aircraft to be redesigned in this work consists of a fixed-wing RPAS to be used for surveillance and agricultural purposes. In its initial version, the propulsion system of the RPAS was a two-cylinder, two-stroke gasoline reciprocating engine driving a two-bladed fixed pitch propeller with a range of 60 min (cruise phase). In 2020, the gasoline-based propulsion system was transformed into a 100% battery-based electric one [8], increasing its autonomy up to 90 min (cruise phase). Now, in this article, the authors go a step further and address the hybrid version of the hydrogen and battery-based propulsion system. Table II shows the standard flight profile of the fixed-wing RPAS subject of this work. From this, it can be seen that of the four phases that compose the flight profile, only the first three have energy requirements.

Analyzing power and energy columns in Table II, it is noted that for the ascent phases 1 and 2, there is a high-power demand for a short period of time, while for cruise phase, the peak power demand is considerably lower than in the ascent phases 1 and 2 (1/7 and 1/5, respectively), and it is required to be maintained over a long period of time (90 min). Therefore, it is reasonable to state that a hybrid electrical propulsion system based on the mix hydrogen-battery would be the most suitable solution.

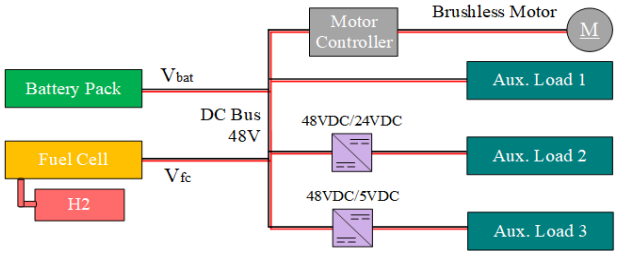


Fig. 2. Electrical propulsion system diagram.

## III. ELECTRICAL DESIGN

The first step in the design of the hybridized propulsion system is to analyze the technical characteristics of each type of energy storage system advisable for RPAS applications. The target is to reduce as most as possible the weight and the space needed for the electrical propulsion system inside the aircraft chassis. Regarding Table II, two different energy phases can be observed in a standard flight of the fixed-wing RPAS. The first one is a high-power demand for a short period of time, corresponding to the ascent phases. For these ascent phases, a battery system would be suitable to provide the required energy and power. The second one is a low-power demand for a long period of time during the cruise phase, for which a hydrogen-powered FC will be used. Next step in the electrical design is to define and draw the diagram of the hybridized hydrogen-based propulsion system, attending to the RPAS necessities. Fig. 2 shows the hybridized hydrogen-based propulsion system, consisting of a proton exchange membrane (PEM) FC and a battery pack, powering the brushless motor and auxiliary loads.

The dc bus is needed to establish a 48 VDC-fixed point, defined by a direct connection of the battery pack. This direct connection avoids the use of a high-power dc/dc converter, reducing weight and cost.

This direct connection is known as "passive control," and the battery pack fixes the voltage at the output of the PEM FC. To ensure safe performance during take-off and double the range from 90 to 180 min, the battery pack and FC have been sized to meet the electrical requirements shown in Table III.

### A. FC System—BoP Design

The balance of plant (BoP) in the PEM FC system is defined as the set of elements which provides the proper support for PEM FC performance, and it can be divided into five main subsystems: 1) hydrogen supply subsystem; 2) oxygenation subsystem; 3) cooling subsystem; 4) electrical subsystem; and 5) control subsystem [9]. In air-cooled PEM FC systems like the one that is proposed for this application, it is possible grouping oxygenation and cooling subsystems, to reduce the number of components.

TABLE III
ELECTRICAL REQUIREMENTS

| Electrical requirements for a flight autonomy of 90 minutes (minimum power requirements) | | | | | |
|---|---|---|---|---|---|
| **Phase** | **t (min)** | **Power (kW)** | **Total Energy (J)** | **Output Voltage (V)** | **Provided by** |
| Ascent 1 | 0.6 | 3.9 | $4.31\times10^5$ | 48 | Battery |
| Ascent 2 | 1.8 | 2.7 | | | |
| Cruise | 82.9 | 0.54 | $2.6\times10^6$ | 48 | Fuel Cell |
| **Electrical requirements for a flight autonomy of 180 minutes (maximum power requirements)** | | | | | |
| **Phase** | **t (min)** | **Power (kW)** | **Total Energy (J)** | **Output Voltage (V)** | **Provided by** |
| Ascent 1 | 0.6 | 4.0[(1)] | $4.35\times10^5$ | 48 | Battery |
| Ascent 2 | 1.8 | 2.7 | | | |
| Cruise | 172.9 | 1.0[(2)] | $10.3\times10^6$ | 48 | Fuel Cell |

[(1)] Battery power upgraded to 4.0 kW from the initial 3.91 kW.
[(2)] Rated power of the fuel cell upgraded to 1.0 kW, from the initial 0.54 kW, to ensure recharging of the on-board battery during the cruise phase (200 W) and to guarantee the extra power (oversizing factor = 1.35) demanded by the RPAS when flying in adverse conditions (1000 W = 1.35×740 W).

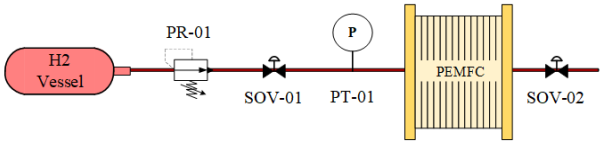


Fig. 3. Fuel supply subsystem configuration.

*1) Hydrogen Supply Subsystem:* The hydrogen supply subsystem must include at least, a hydrogen vessel, a manual pressure regulator (PR-01) a control supply valve (SOV-01), a pressure transmitter (PT-01), and a purge valve (SOV-02), Fig. 3. If the PEM FC allows recirculation of excess hydrogen to the anode, it is called flowthrough anode (FTA), and if there is no recirculation, it is called dead-ended anode (DEA). In this case, the DEA configuration has been chosen due to its simplicity and weight reduction. On the other hand, it has been observed in [9] that if the hydrogen or oxygen input flows rates are reduced, the stack power drops to 0 W due to the "fuel starvation" phenomenon. While if the input flow rate is increased, no difference is noticed with respect to the nominal flow rate values.

It is also necessary to size the capacity of the hydrogen vessel based on the maximum PEM FC power ($P_{\text{fc}} = 1000$ W) and the desired autonomy (180 min = 3 h). The hydrogen tank should be sized to store at least the energy that after electrochemical conversion by the FC, the available electrical energy provided by the PEM FC system should be $E_{\text{fc}} = 3000$ Wh. Regarding energy contained in hydrogen, it can be estimated by averaging its lower and upper heating values for the following equation:

$$AHV_{H2} = \frac{LHV_{H2} + HHV_{H2}}{2} \tag{1}$$

where

$AHV_{H2}$ average heating value of hydrogen (kJ/kg);
$LHV_{H2}$ lower heating value of hydrogen (120 kJ/g);
$HHV_{H2}$ higher heating value of hydrogen (142 kJ/g).

Resulting $AHV_{H2} = 131$ (KJ/g) = 36.38 (Wh/g).

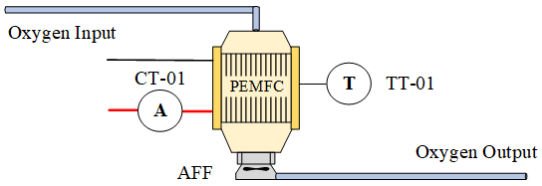


Fig. 4. Oxygenation and cooling subsystem configuration.

Furthermore, the average PEM FC efficiency can be estimated on 40%, and assuming that it can decrease by 10% due to power electronics (dc/dc converter on Fig. 2), it can be considered PEM FC efficiency of $n_{\text{fc}} = 30\%$. Then, the hydrogen mass required to guarantee the required energy is given by the following equation:

$$m_{H2} = E_{\text{fc}} \cdot \frac{1}{AHV_{H2} \cdot n_{\text{fc}}} \tag{2}$$

where

$m_{H2}$ hydrogen mass required to guarantee the energy required by the PEM FC (g).

Resulting $m_{H2} = 274.87$ g.

According to the analysis of hydrogen storage options carried out in [10], authors propose to use a high-pressure type IV hydrogen tank, which must store 275 g of hydrogen, weighting at most 3 kg and having a diameter and length smaller than 150 and 500 mm, respectively.

*2) Oxygenation and Cooling Subsystem:* In air-cooled PEM FC, oxygenation and cooling subsystems are integrated as one single subsystem into the same structure, reducing the weight and volume. Knowing that the most efficient way of providing the airflow to the PEM FC system is by using only one fan-out and a tapered structure, this subsystem must contain at least an adjustable flow fan (AFF), a tapered structure, a current transmitter (CT-01), a temperature transmitter (TT-01), and a connection system, as shown in Fig. 4. In addition, it can be noted that an open cathode and anode configuration has been used, with the aim of reducing even more the components needed. In this way, to ensure the right grant, it is necessary to calculate the most restrictive value between the oxygenation and refrigeration requirements.

*a) Oxygenation mass flow:* The mass flow needed for the stoichiometric reactions inside the PEM FC can be calculated with the following equation:

$$\dot{m}_{\text{O2}} = \frac{I_{\text{fc}} \cdot N_{\text{cell}}}{4 \cdot \text{F}} \tag{3}$$

where

$\dot{m}_{\text{O2}}$ oxygen molar flow (mol/s);
$I_{\text{fc}}$ electrical current provided by the PEM FC (A);
$N_{\text{cell}}$ number of cells in the stack;
F Faraday constant (96 485 C/mol).

On the other hand, the PEM FC system power can be calculated as follows:

$$P_{\text{fc}} = V_{\text{cell}} \cdot I_{\text{fc}} \cdot N_{\text{cells}}. \tag{4}$$

Considering the oxygen/air concentration rate is $X_{\text{O2/Air}} = 21\%$, and the average air molar mass value is

$M_{air} = 28.79$ g/mol, the resultant air mass flow requirements is given by the following equation:

$$\dot{m}_{air_{oxy}} = \frac{P_{fc} \cdot M_{air}}{4 \cdot F \cdot V_{cell} \cdot X_{O2/Air} \cdot \lambda_s} \quad (5)$$

where

| | |
|---|---|
| $\dot{m}_{air_{oxy}}$ | air mass flow needed for oxygenation (kg/s); |
| $M_{air}$ | average air flow mass (28.79 g/mol); |
| $V_{cell}$ | cell voltage ($V$); |
| $X_{O2/Air}$ | oxygen/air rate (21%); |
| $\lambda_s$ | stoichiometric coefficient ($\lambda_s = 2$). |

At the maximum power point PEM FC operation, $V_{cell} = V_{cell_{mp}} = 0.6$ V and $P_{fc} = 1000$ W, resulting $\dot{m}_{air_{oxy}} = 0.29$ g/s.

*b) Cooling mass flow:* From the total heat energy produced by the PEM FC, approximately 40% must be removed by forced convection, as the remaining 60% will be transmitted through conduction or radiation to other surfaces of the platform.

Heat generated by the PEM FC system, $Q_{fc_g}$, and evacuated heat energy, $Q_{fc_e}$, can be calculated from the following equation:

$$Q_{fc_g} = P_{fc} \cdot \left(\frac{1.25}{V_{cell}} - 1\right) \quad (6)$$

$$Q_{fc_e} = \dot{m}_{air_{cool}} \cdot C_p \cdot \Delta T \quad (7)$$

where

| | |
|---|---|
| $Q_{fc_g}$ | heat generated by the PEM FC (W); |
| $Q_{fc_e}$ | heat to be evacuated to cool the PEM FC (W); |
| $\dot{m}_{air_{cool}}$ | air mass flow required to evacuate the generated heat (Kg/s); |
| $C_p$ | air heat capacity (1004 J/(Kg · s)); |
| $\Delta T$ | temperature difference between the operating temperature of the PEM FC and the air temperature (°C). |

Considering the air temperature as 25 °C, the operating temperature as 60 °C, and replacing the design parameters calculated previously, the resultant air-cooling mass flow is given by the following equation:

$$\dot{m}_{air_{cool}} = \frac{P_{fc} \cdot \left(\frac{1.25}{V_{cell}} - 1\right) \cdot 0.4}{C_p \cdot \Delta T}. \quad (8)$$

Resulting $\dot{m}_{air_{cool}} = 12.33$ g/s.

Then, comparing result from (5) and (8), it can be determined that the most restrictive air mass flow requirement is the cooling airflow ($\dot{m}_{air_{cool}} = 12.33$ g/s $> \dot{m}_{air_{oxy}} = 0.29$ g/s). According to this value, fan model OD9225-48LBXE from ORION FANS has been selected.

*3) Electrical and Control Subsystem:* Facing the electrical subsystem, it must ensure the correct connection with the rest of elements. Then, an antireturn diode and a power relay (RLY) are needed. Also, the information required for the correct control of the system will be provide by a voltage transmitter (VT-01) and a current transmitter (CT-01), as shown in Fig. 5.

On the other hand, the control subsystem must manage the behavior of all devices that integrate the BoP of the PEM FC. For this task, a microcontroller (Arduino Nano) is used, which stands out for its low consumption and reduced dimensions in cooperation with optocouplers.

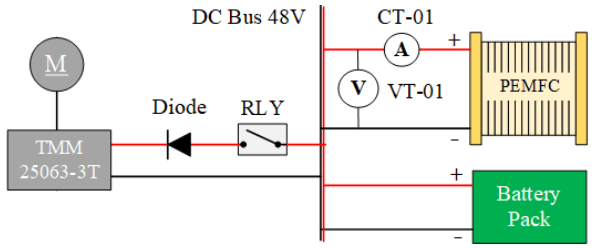


Fig. 5. Electrical subsystem configuration.

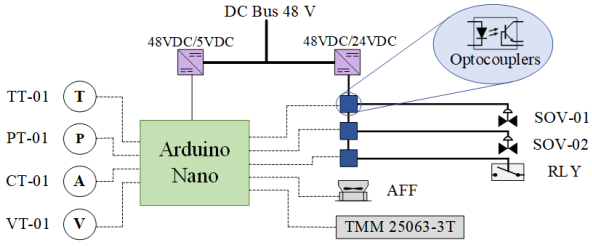


Fig. 6. Control subsystem configuration.

It is also necessary to include a 48/24 VDC converter and a 48/5 VDC converter to power the BoP elements from the 48 VDC bus, Fig. 6.

### *B. Battery Pack Design and Sizing*

As it has been described above, Fig. 2 shows the integration of the battery pack into the hybridized hydrogen-based propulsion system. The energy requirements that the battery pack must meet are listed in Table II. Before starting to size the battery pack, it is needed to analyze the options and technologies available, choosing the most suitable one. According to the analysis of the main characteristics of each battery family done in [11], and taking into account that the goal of the battery pack would be to supply the take-off energy needed by the RPAS, a Li-Ion battery has been chosen.

The total energy that the battery pack can store is given by (9)

$$E_{bat} = \int_0^t V_{bat} \cdot I_{bat} = C_{bat} \cdot V_{bat} \quad (9)$$

where

| | |
|---|---|
| $E_{bat}$ | energy to be provided by the battery pack (see Table III); |
| $V_{bat}$ | battery voltage (48 V); |
| $I_{bat}$ | battery current (A); |
| $C_{bat}$ | battery capacity (Ah). |

And the maximum power that the battery is able to provide depends on the $c_{rating}$, according to the following equation:

$$P_{bat} = C_{bat} \cdot V_{bat} \cdot c_{rating} \quad (10)$$

where

| | |
|---|---|
| $P_{bat}$ | maximum power to be provided by the battery pack (4000 W, Table III); |
| $c_{rating}$ | discharging coefficient of the battery ($h^{-1}$). |

TABLE IV
ELECTRICAL DESIGN. COMPONENTS SELECTION

| System | Subsystem | Component |
|---|---|---|
| Fuel Cell | Hydrogen supply | - SOV-01: Burkert Type 6011A<br>- SOV-02: Burkert Type 6011A<br>- PR-01: DVS-020-VH-AP4<br>- PT-01: WIKA S-20 - 14071135<br>- H2 vessel: Type IV, 275 g $H_2$, 3.0 Kg, Ø150 mm, L 500 mm. |
| | Oxygenation and Cooling | - AFF: OD9225-48LBXE ORION<br>- TT-01: CS241 Temperature sensor |
| | Electrical and control | - Diode: VS-1N3290R<br>- RLY: SENSATA/CRYDOM D06D100<br>- VT-01: Author custom design<br>- CT-01: LEM AK 50 C420L<br>- Controller: Arduino Nano<br>- Optocouplers: FOD3182 3A<br>- 48 VDC/24 VDC 5A converter<br>- 48 VDC/5 VDC 1A converter |
| Battery Pack | | - Battery pack: 13s2p LPHD1170170 |
| Engine | | - Controller: TMM 25063-3T.<br>- Motor: DC Plettenberg Predator 37-6 |

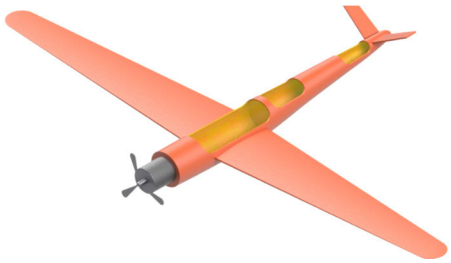

Fig. 7. Estimation of available weight and volume based on 3-D simulation.

Noticing that the brushless motor installed into the fixed-wing RPAS has a nominal voltage of 48 V and taking into account (9) and (10), the capacity and discharging rate of the battery pack must be, at least, 25 Ah and 3.33 $h^{-1}$, respectively. According to these values, a commercial battery pack in 13s2p configuration made with LPHD1170170 lithium polymer batteries has been selected.

Table IV shows the selected components for each subsystem. The criteria followed for components choice are: 1) electronic and instrumentation compatibility and 2) weigh and volume. That is, the control and instrumentation subsystem has been designed based on three voltage reference levels: 48 VDC from the power electronics, 24 VDC for actuators (valves and relays), and 5 VDC for transmitters. Based on the compliance with these electronics and instrumentation compatibility constrains, components have been selected based on commercial availability and the lowest weight and volume.

## IV. MECHANICAL SIZING

For the mechanical sizing, it is necessary to have a precise knowledge of the available space and weight. According to specifications taken from [8], a 3-D simulation of the RPAS casing has been conducted, as shown in Fig. 7. From the 3-D simulation, it is possible to know that the MTOW and volume available for the hydrogen-based propulsion system would be 25 kg and 29.22 $dm^3$, respectively.

Based on electrical requirements (see Fig. 2 and Table II), and weight, space, and dimensions available (see Fig. 7) to integrate the hydrogen-based propulsion system, and regarding the commercial availability of FCs system, authors have not found any commercial FC system that meets both electrical and mechanical specifications. Then, authors present a design for a customized FC system that meets the requisites to implement the hydrogen-powered fixed-wing RPAS.

### A. FC System Sizing

Regarding the environmental and operating conditions, PEM FC technology is selected [12]. To start the mechanical sizing of the PEM FC system, we will pay attention to previous electrical design. According to Fig. 2, the voltage provided by the FC system must be $V_{\text{fc}} = 48$ V. On the other hand, the theorical voltage provided by a single cell can be consider as $V_{\text{cell}_{\text{theorical}}} = 1.23$ V, however, due to the nonidealities of a real system, this voltage decreases to $V_{\text{cell}_{\text{real}}} = 0.9$ V and, finally, in case of voltage measurement at maximum power operating point, the usual value obtained is $V_{\text{cell}_{p\_\max}} = 0.6$ V.

For the PEM FC stack assembly, it is possible to connect the cells in series, in parallel, or in a mixed way. In this case, a series connection has been chosen in accordance with the elongated geometry of the aircraft. Therefore, the number of cells needed to implement the PEM FC stack to meet with electrical design requirements, can be calculated with the following equation:

$$N_{\text{cells}} = \frac{V_{\text{fc}}}{V_{\text{cell}_{p\_\max}}} \tag{11}$$

where

$N_{\text{cells}}$ number of cells of the PEM FC stack;
$V_{\text{fc}}$ voltage at the terminals of the PEM FC system (48 V);
$V_{\text{cell}_{p\_\max}}$ cell voltage operating at max. power (0.6 V).

Resulting $N_{\text{cells}} = 80$ cells.

Taking into account the maximum power value stablishes for the cruise phase, $P_{\text{fc}} = 1000$ W (see Table II), the active area of cell can be calculated using the following equation:

$$A_{\text{active}} = \frac{P_{\text{fc}}}{V_{\text{cell}_{mp}} \cdot N_{\text{cells}} \cdot \delta_{\text{Current}_{\text{MEA}}}} \tag{12}$$

where

$P_{\text{fc}}$ power supplied by the PEM FC system (W);
$\delta_{\text{Current}_{\text{MEA}}}$ membrane electrode assembly (MEA) current density (A/$cm^2$).

Using a conservative value $\delta_{\text{Current}_{\text{MEA}}} = 0.4$ (A/$cm^2$) [13], the active area of the cell needed would be $A_{\text{active}} = 52$ $cm^2$. Considering borders in the bipolar plates (BPs), please see Section IV-B, the total area of the cell and BPs, will be $A_{\text{cell}} = A_{\text{BP}} = 81$ $cm^2$, and the final BP dimensions as shows Fig. 8.

### B. BPs Design and Sizing

For the mechanical design of the BPs, the main aspects that must be considered are listed below.

*1) BPs Material:* To choose a suitable material, it is necessary to know the requirements to be met and its functions

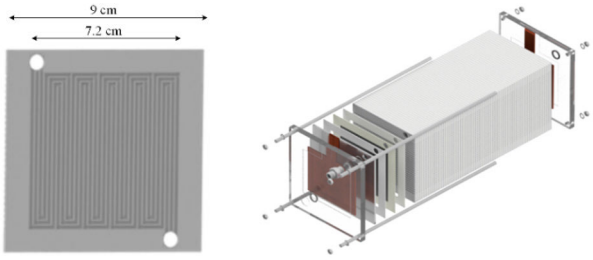


Fig. 8. FC stack. Sizing and packing.

TABLE V
BPs Design Parameters

| | |
|---|---|
| BPs material | Non porous graphite |
| Flow channels pattern | Serpentine pattern |
| Flow direction | Counter-flow |
| Flow channel geometry | Rectangular cross-section |
| Anode channels/ribs width/height | Width/Height: 1.0/0.5 mm |
| Cathode channels/ribs width/height | Width/Height: 2.0/1.5 mm |

within the system. The main functions of BP are to supply the fuel and oxidant agents, to evacuate the water generated at the cathode and heat, to transport electrons to the collectors, and to provide structural integrity to the stack.

Therefore, to evaluate a material as suitable for use in the manufacture of BPs, [14] establishes the following minimum criteria that must be met: electrical conductivity $>100$ S $\cdot$ cm$^{-1}$; contact resistance $\leq 20$ m$\Omega \cdot$ cm$^2$ at 140 N/cm$^2$; thermal conductivity as high as possible; hydrogen/gas permeability $<10$–$4$ cm$^3$/(s$\cdot$cm$^2$); corrosion resistance $<0.016$ mA/cm$^2$; compressive strength $>0.1517$ MPa; flexural strength $\geq 59$ MPa; mass density $<5$ g/cm$^3$.

*2) BPs Flow Channels Pattern:* The aim of the BPs' flow channels study is to reduce as much as possible the pressure drop during the movement through the channel, besides maintaining a high fluid speed, obtaining a homogeneous distribution, and improving the efficiency of the electrochemical reaction. Some flow pattern options are parallel channels pattern, serpentine channels pattern, diaphanous pattern, and bioinspired patterns [15].

*3) BPs Flow Channels Geometry:* Some extra geometry aspects are important to get high-performance. The first one is the flow direction of the fluid. The most usual configuration that can be seen on commercial BPs are co-flow, counterflow, and cross-flow. These three options have been analyzed in [16], concluding that the best performance is obtained with a counterflow geometry, due to a better humidity distribution in the cell.

Table V lists the characteristics and geometries chosen by the author for the proposed FC.

### C. PEM FC Assembly

PEM FC assembly is a key aspect to consider. Not having the proper tightening could lead to a considerable reduction in PEM FC stack performance due to high contact resistance between the GDL and the BP, as well as the risk of water and fuel leakage. On the other hand, overtightening could result in a deterioration of the PEM FC stack and a worsening in the long-term of the PEM FC performance due to plastic deformation inside the stack.

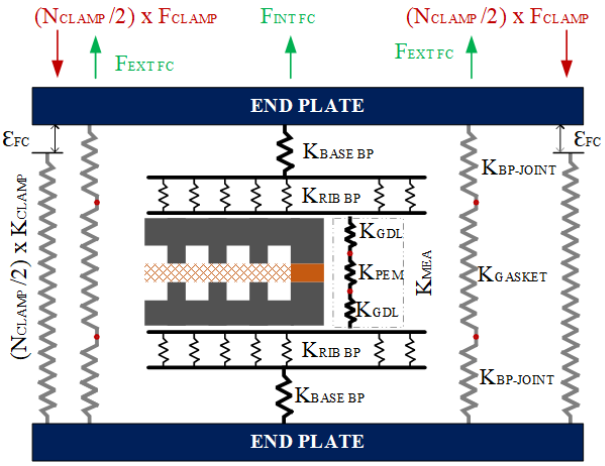


$\varepsilon_{FC}$ = Stack shrinkage (mm)
$K_{BASE\ BP}$ = BP´s base equivalent stiffness ($8.00 \cdot 10^7$ N/mm)
$K_{RIB\ BP}$ = BP´s rib equivalent stiffness ($2.08 \cdot 10^6$ N/mm)
$K_{JOINT\ BP}$ = BP´s joint equivalent stiffness ($18.40 \cdot 10^6$ N/mm)
$K_{GDL}$ = GDL equivalent stiffness ($27.39 \cdot 10^4$ N/mm)
$K_{PEM}$ = PEM equivalent stiffness ($37.40 \cdot 10^6$ N/mm)
$K_{MEA}$ = MEA equivalent stiffness ($13.64 \cdot 10^4$ N/mm)
$K_{GASKET}$ = Gasket equivalent stiffness ($12.04 \cdot 10^2$ N/mm)
$K_{CLAMP}$ = Clamp equivalent stiffness ($1.76 \cdot 10^4$ N/mm)
$N_{CLAMP}$ = Number of clamps used (4 clamps)
$F_{CLAMP}$ = Force applied by each clamp (N)
$F_{INT\ FC}$ = Force applied by the internal fuel cell (N)
$F_{EXT\ FC}$ = Force applied by the external fuel cell (N)

Fig. 9. Spring model of the PEM FC proposed for the RPAS.

For the case under study, a spring model has been developed, analyzing each component separately and considering its elastic modulus ($E$), lineal thermal expansion coefficient ($\alpha$), and geometry. By using the following equation, it is possible to calculate their equivalent stiffness ($K$) and thermal expansion ($\varepsilon_{\text{thermal}}$):

$$K = \frac{E \cdot A}{L} \tag{13}$$

$$\varepsilon_{\text{thermal}} = \alpha \cdot \Delta T \cdot L \tag{14}$$

where

| | |
|---|---|
| $K$ | equivalent stiffness (MPa $\cdot$ mm); |
| $E$ | elastic modulus (MPa); |
| $A$ | element cross-sectional area (mm$^2$); |
| $L$ | element length (mm); |
| $\alpha$ | lineal thermal expansion coefficient (K$^{-1}$); |
| $\Delta T$ | temperature variation between ON and OFF (°C). |

The spring model used for the tightening estimation is shown in Fig. 9.

Considering the difference in magnitude between the equivalent stiffness of the gasket and the other components, it can be assumed that the main deformation will occur in that element and the force to be exerted will be that necessary to deform the gasket until it plugs all possible hydrogen escape routes.

Therefore, applying the expressions in the following equation and setting a desired deformation of 0.5 mm in the

gasket (gasket thickness 2 mm and groove depth 1.5 mm), the torque required to tighten the bolts can be estimated:

$$F_{\text{preload}} = \varepsilon_{\text{FC}} \cdot K \tag{15}$$

$$T_{\text{clamp}} = F_{\text{preload}} \cdot \mu_{\text{friction}} \cdot \emptyset_{\text{clamp}} / N_{\text{clamp}} \tag{16}$$

where

$F_{\text{preload}}$ force applied to compress the stack ($N$);
$\varepsilon_{\text{FC}}$ stack shrinkage (mm);
$T_{\text{clamp}}$ required torque on each clamp (Nm);
$\mu_{\text{friction}}$ clamp friction coefficient (0.2);
$\emptyset_{\text{clamp}}$ clamp nominal diameter (6 mm);
$N_{\text{clamp}}$ number of clamps used (four clamps).

Resulting in a required torque on each clamp of the FC of $T_{\text{clamp}} = 0.24$ Nm.

### D. Center of Mass Checking

To ensure the stability and feasibility of the hydrogen-powered fixed-wing RPAS, the real position of the center of mass has been calculated and compared with the theoretical center of mass. The goal is to verify that the difference between the real and the theoretical center of mass falls within the established safety range for the proposed RPAS.

The theoretical center of mass has been located based on the aerodynamic characteristics of the platform. The existing symmetry of the aerial platform in the vertical and transversal axes means that most attention is focused on the longitudinal axis, which is the most important in the flight profile.

On the other hand, the center of mass of the complete hydrogen-based system has been calculated from the location and individual weights of each component, as shown in Table VI.

Therefore, the position of the ideal center of mass is located at $x, y, z(\text{mm}) = \{567, 0, 0\}$, while the position of the real center of mass is located at $x, y, z(\text{mm}) = \{563.90, -1.80, 3.60\}$, as shown in Fig. 10.

This result ensures a center of mass location within the safe range, being slightly beyond, which increased the longitudinal stability of the platform.

Furthermore, the total weight of the system has been calculated based on the weight of all equipment selected (please see Sections IV-A–IV-D). The estimated final weight is 23.63 kg (based on our experience, we believe that in the prototyping phase, this weight can be lowered). Considering that the maximum take-off weight of the designed RPAS is 25 kg, it results on 1.37 kg for payload.

TABLE VI
HYDROGEN-BASED PROPULSION SYSTEM. WEIGHT DISTRIBUTION AND COMPONENTS' LOCATION

| Subsystem | Component | Weight (g) | [X, Y, Z] location (mm) |
|---|---|---|---|
| Fuel Cell | Stack | **5185** | [597.50, 0, 8] |
| Battery pack | LPHD1170170 | **6040** | [347.80, -19.40, -10.50] |
| Platform casing, engine and steering elements | RPAS casing | 3500 | [847, 0, 0] |
| | Motor and controller | 3890 | [132, 16.40, 0] |
| | Propeller | 300 | [35, 0, 0] |
| | Telemetry module | 180 | [290.40, 15.70, 5.30] |
| | Fly Control System (FCS) | 275 | [278.30, 5.60, 2.10] |
| Subtotal | | **8145** | |
| Hydrogen supply subsystem | Parachute | 250 | [1575.2, 0, 59.72] |
| | H2 Vessel | 3000 | [1118.4, 0, 32.01] |
| | SOV-01 | 120 | [937.2, 57.6, 43.1] |
| | SOV-02 | 120 | [814.10, -48.30, -33.40] |
| | PR-01 | 200 | [1034.30, 0, 10.40] |
| Subtotal | | **3690** | |
| Oxygenation and cooling subsystem | PT-01 | 75 | [777.30, -44, -23.10] |
| | TT-01 | 30 | [597.50, 0, 8] |
| | CC-01 | 20 | [602.70, 3.20, -10.90] |
| | AFF | 70 | [597.50, 70, 8] |
| | Piping | 200 | [748.60, 0, 0] |
| Subtotal | | **395** | |
| Electrical and control subsystem | Arduino Nano | 20 | [272.10, -43.60, 0] |
| | Diode | 25 | [320, 22.70, -45.20] |
| | RLY | 35 | [306.40, 22.40, -41.40] |
| | VT-01 | 20 | [597.50, 40, 8] |
| | Optocouplers | 5 | [378, -38.40, -32.40] |
| | 48VDC/24VCD | 42 | [356, 32.60, -64.50] |
| | 48VDC/5VCD | 27 | [334, 41.90, -63.70] |
| Subtotal | | **174** | |
| **Total weight (kg)** | | **23.62** | |
| **Centre of mass [x,y,z] mm** | | | **[563.90, -1.80, 3.60]** |

## V. AERODYNAMICS AIR INTAKES ANALYSIS

The objective when designing air intakes on an aircraft is to ensure that the flow to the element to be cooled or oxygenated (that is the FC) is as uniform as possible, with a constant pressure and without significantly affecting the overall aerodynamics of the aerial platform [17].

Most of the problems that occur when designing an air intake are related to the proximity of the inlet, as this is the point where the separation between the internal flow and the external flow occurs. Depending on the operating speed of the aircraft, the design of the air intakes varies and can be classified into subsonic air intakes (<343 m/s) and supersonic air intakes (>343 m/s). From [9], it is known that the RPAS's top speed is 32 m/s, so it undoubtedly belongs to the subsonic regime, and the air intakes will have to be sized accordingly. Finally, from Bernoulli's equation, it is deduced that a gas is incompressible if its velocity is less than 102.90 m/s [18]. For the design of the air intake, it will use this approximation to facilitate the associated calculations. Fig. 11 shows the types of air intakes most used in the subsonic regime.

Authors propose a variant of pitot model, as shown in Fig. 12. This proposal is based on two principles: aerodynamics and FC system.

1) Aerodynamics principle:
   a) Under subsonic operating conditions, this type of air intake performs adequately, without significantly affecting the aerodynamics of the aircraft.
   b) This air intake design will make it easier to implement the air intake in an existing platform.

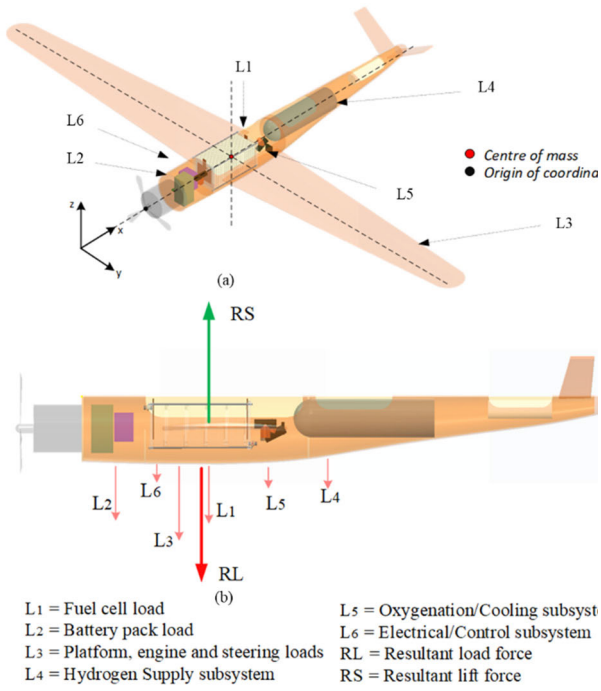


Fig. 10. (a) Load distribution and center of mass into the RPAS. (b) Load and lift forces resultant.

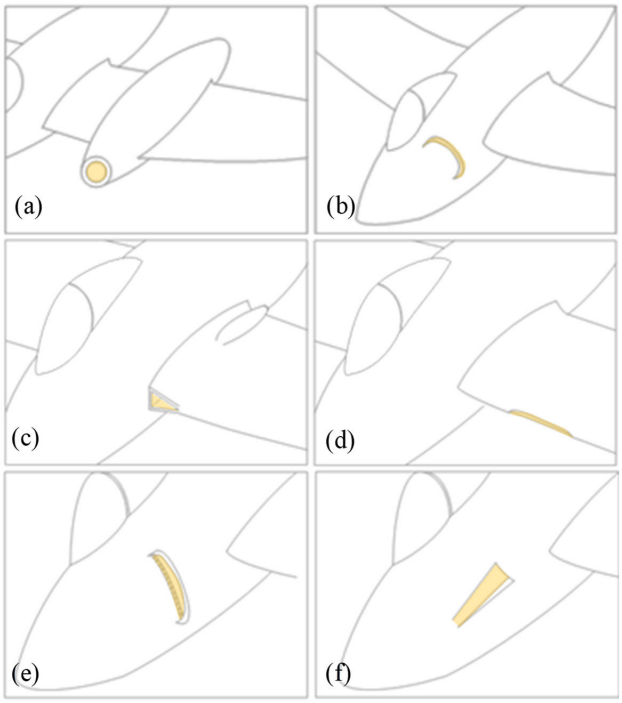


Fig. 11. (a) Pitot intake. (b) Lateral without boundary layer suction intake. (c) Wing root intake. (d) Leading edge intake. (e) Lateral with boundary layer suction intake. (f) NACA intake.

2) FC system principle:

a) The RPAS is powered by a hydrogen-based propulsion system located inside the fuselage. Therefore, it is recommended to place the air intake at the front while maintaining the pitot geometry in order to guarantee the oxidizer/cooling requirements.

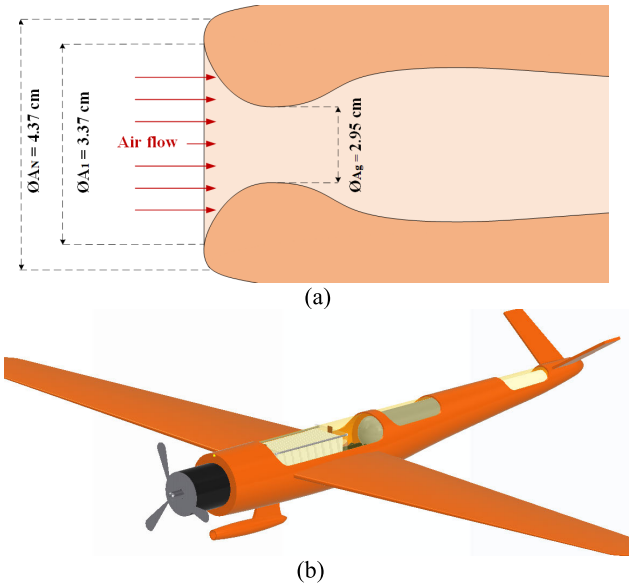


Fig. 12. (a) Duct cross-sectional area profile. (b) Pitot intake location.

TABLE VII
AIR INLET PREDIMENSIONING DESIGN VALUES

| Mass flow ($m_{air}$) | Max. Speed ($v_{max}$) | Cruise Speed ($v_{cruise}$) | Air density ($\delta_{air}$) |
|---|---|---|---|
| $1.23 \cdot 10^{-2}$ kg/s | 70 m/s | 32 m/s | 1.14 kg/m$^3$ |

* *Air density has been calculated, assuming a flight altitude of 720 m.*

b) This is intended to reduce the pressure drop that may occur in the oxygenation duct and to reduce the space and weight associated with the ducts. In addition, this position on the symmetry axis reduces the possible asymmetries that could be caused by another location in the aerodynamics of the aircraft.

Once the air intake design has been justified, next steps would be listed.

*Step 1 (Predimensioning):* For the pre-dimensioning, the requirements of the fuel cell, the characteristics of the type of flight performed by the platform and the restrictions due to the rest of the system elements are considered, Tables II and IV.

*Step 2 (Aerodynamic Tunnel Test):* This step is carried out simulating flow ratios and extracting their influence on the recovery of pressures and distortion in the various configurations.

*Step 3 (Flight Test):* This step would involve testing the aircraft prototype on a test bench real aircraft to verify theoretical predictions, compare results, and make final modifications to the design.

Within the predimensioning phase, the recommended procedure would be the following. From the cooling requirement (the mass flow required for oxygenation/cooling) and the flight speed given in Table VII, estimate the critical throat area using the following equation:

$$\dot{m}_{\text{air}} = \frac{\delta_{\text{air}} \cdot A_g \cdot v_{\text{cruise}} \cdot \text{sen}(\alpha)}{\beta} \tag{17}$$

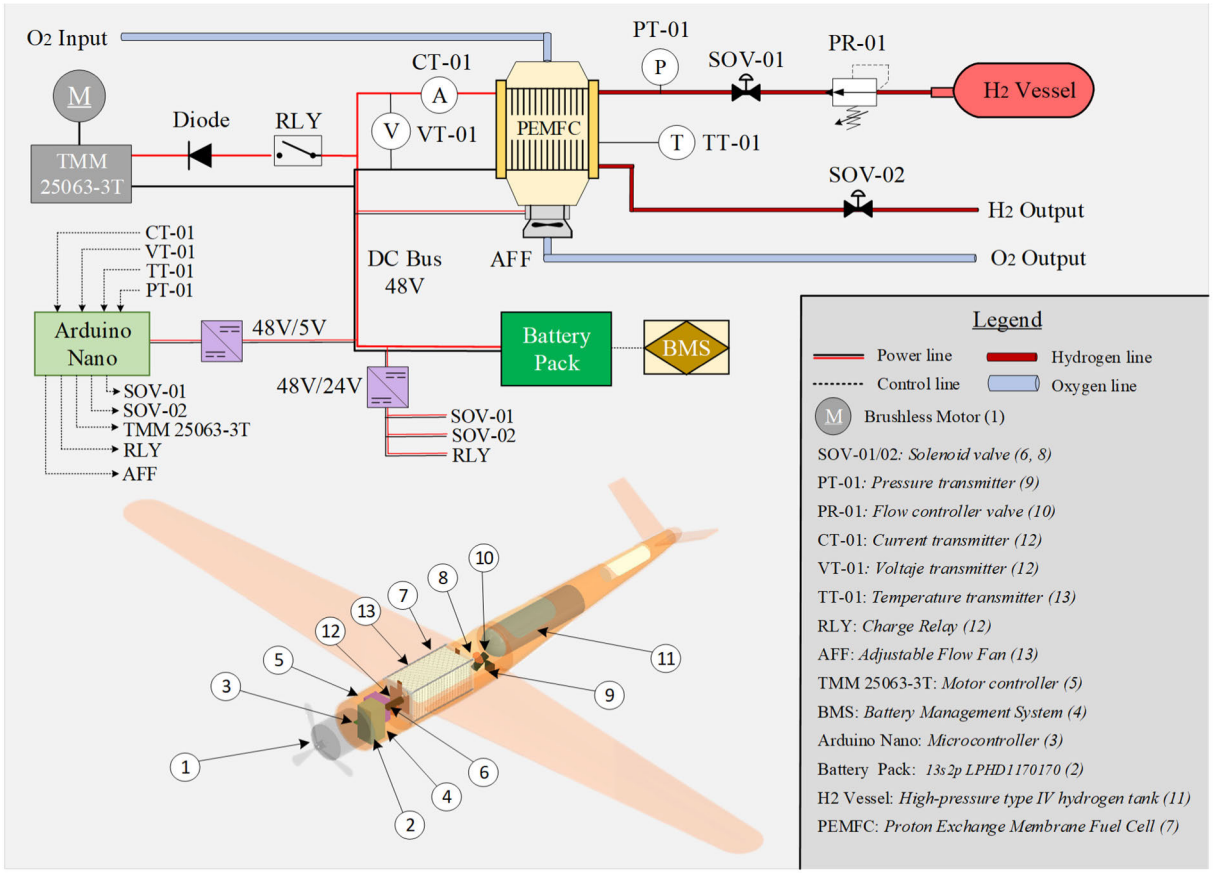


Fig. 13. Proposed hydrogen-powered RPAS: electrical design and internal equipment distribution.

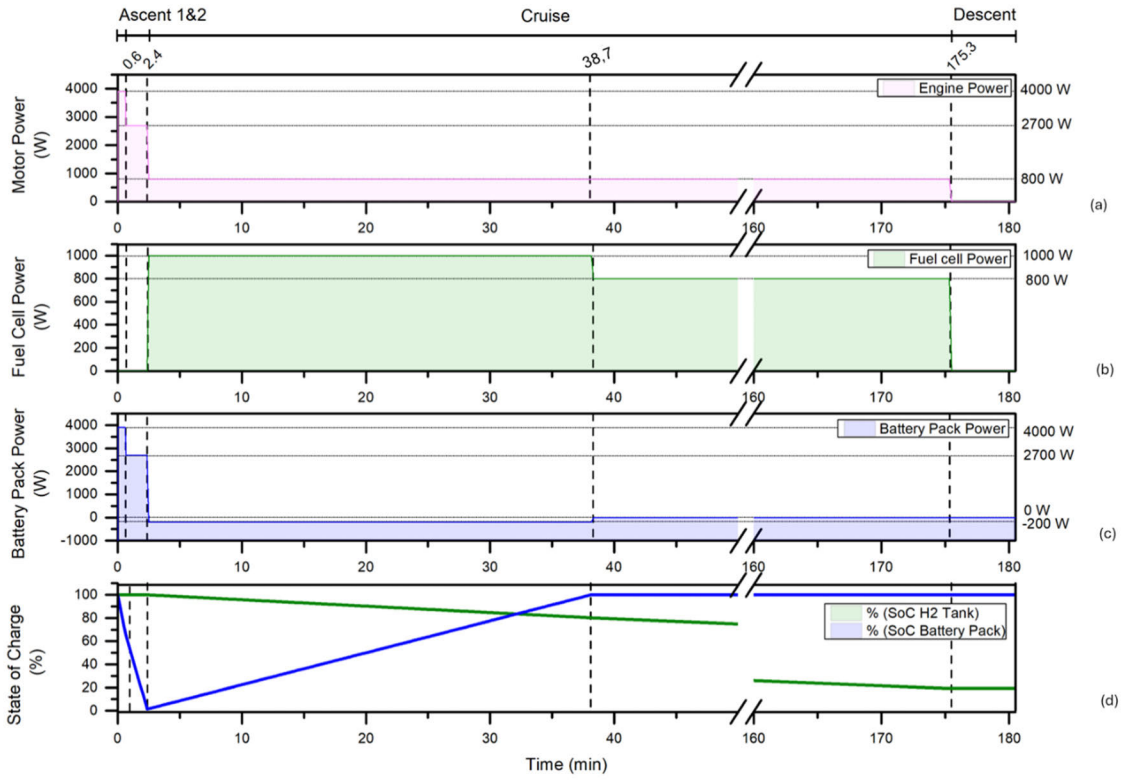


Fig. 14. Simulation results (a) engine power, (b) FC power, (c) battery power, and (d) state of charge.

TABLE VIII
HYDROGEN-POWERED FIXED-WING RPAS PROPULSION SYSTEM COMPONENTS

| Subsystem | Components and technical details |
|---|---|
| **Fuel Cell** | |
| Hydrogen supply | - SOV-01: Burkert Type 6011A<br>- SOV-02: Burkert Type 6011A<br>- PR-01: DVS-020-VH-AP4<br>- PT-01: WIKA S-20 - 14071135<br>- H2 vessel: Type IV, 253 g $H_2$, 3.0 Kg, Ø150 mm, L 500 mm. |
| Oxygenation and Cooling | - AFF: OD9225-48LBXE ORION<br>- TT-01: CS241 Temperature sensor<br>- CT-01: LEM AK 50 C420L |
| Electrical and control | - Diode: VS-1N3290R<br>- RLY: SENSATA/CRYDOM D06D100<br>- VT-01: Author custom design<br>- Controller: Arduino Nano<br>- Optocouplers: FOD3182 3A<br>- 48V/24V 5A and 48V/5V 1A converter (DC) |
| Stack | - Number of cells: 80<br>- BPs dimensions: 90x90x3mm<br>- BPs material: Non-Porous graphite<br>- Flow channels pattern: Serpentine<br>- Flow direction: Counter-flow<br>- Flow channel geometry: Rectangular<br>- Anode channels/ribs width/heights: 1/0.5 mm<br>- Cathode channels/ribs width/heights: 2/1.5 mm<br>- Number of clamps: 4<br>- Tightening torque on clamps: 0.24Nm |
| **Battery Pack** | |
| - Battery pack: 13s2p LPHD1170170 | |
| **Engine** | |
| - Controller: TMM 25063-3T.<br>- Motor: DC Plettenberg Predator 37-6 Brushless. | |
| **Air intake** | |
| - Pitot style inlet<br>- Critical throat ($\emptyset A_g$) = 2.95 cm<br>- Intake inlet area ($\emptyset A_1$) = 3.37 cm<br>- External profile area ($\emptyset A_N$) = 4.37 cm | |

where

$\dot{m}_{\text{air}}$ air mass rate required. From (8), it has been justified that $\dot{m}_{\text{air}} = \dot{m}_{\text{air}_{\text{cool}}} = 1.23 \cdot 10^{-2}$ kg/s;
$\delta_{\text{air}}$ air density (1.14 kg/m$^3$);
$A_g$ area of the critical throat (m$^2$);
$v$ RPAS cruise speed (32 m/s);
$\alpha$ angle between the plane in which the orifice is contained and the path of the air;
$\beta$ safety factor to assume the possibility of turbulent flow or increased relative humidity into the RPAS ($\beta = 2$).

By selecting a Pitot style inlet (which allows the aircraft's airspeed to be measured while simultaneously supplying air to the FC) with an inlet angle perpendicular to the air flow ($\alpha = 90°$) and substituting into the expression (17), the resultant critical throat area is $A_g = 6.83$ cm$^2$.

Next, the intake inlet area ($A_1$) must be defined, which as a general rule [17] (for low-speed aircraft) is estimated as $A_1 = 1.3 \cdot A_g = 8.89$ cm$^2$.

Once the intake inlet area is defined, the outer airfoils of the air intake are also defined. The main condition is to ensure that the "critical match number of the airfoil" is higher than the "resistor divergence match number of the drag" ($v_{\text{rd}}$).

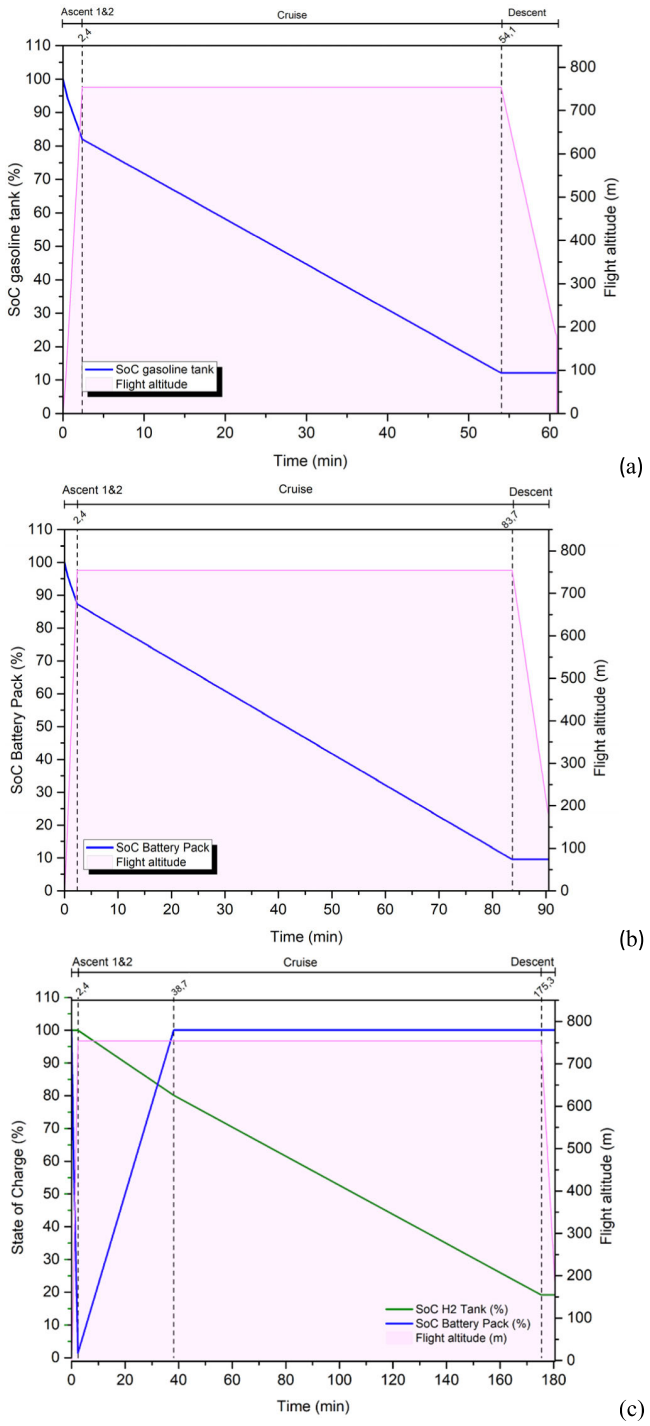


Fig. 15. Achieved autonomy by the RPAS. (a) Gasoline-based engine. (b) Battery-based propulsion system. (c) Hybridized hydrogen-based propulsion system.

The critical match number of the airfoil is influenced by the airspeed of the aircraft, the cost ratio, and the angle of incidence and slip angle ranges [17].

Since the resistor divergence match number is usually around 0.6 Mach (or 205.8 m/s) in the worst case [17], it should be ensured that this speed is not exceeded at the intake inlet, using the following equation:

$$\frac{v_{\text{rd}}}{v_{\max}} = \frac{A_m}{A_1} \tag{18}$$

where

$v_{rd}$ fluid inlet velocity at the intake (205.8 m/s as maximum);
$v_{max}$ maximum fluid velocity outside the tapping range of influence (70 m/s);
$A_m$ maximum resistant area of the air socket.

By substituting the value obtained for $A_1 = 8.89$ cm$^2$, into (18), it is possible to know the maximum resistant area of the air socket as $A_m = 25.93$ cm$^2$.

On the other hand, considering that the resistant area $A_m$ of the air socket is made by intake inlet area, $A_1$, and the external profile area, $A_N$, the following equation can stablish:

$$A_m = A_1 + A_N. \tag{19}$$

Resulting on a maximum $A_N = 7.04$ cm$^2$.

This large drag area is given by the low flight speed of the RPAS ($v_{max}$), making it unlikely to reach critical speeds even with a suboptimal air intake design. Then, the diameter of the inlet port shall be $\emptyset A_1 = 3.37$ cm, while the intake envelope should have a thickness of 5 mm (the same thickness as the rest of the fuselage), which gives an external profile diameter $\emptyset A_N = 4.37$ cm, Fig. 12(a).

Next step is the sizing of the inside of the inlet, i.e., the duct. At the beginning of the duct, the inlet area ($A_1$) is established, and it is then passed from this area to the critical throat area ($A_g$) by using elliptical profiles that cause a significant area reduction.

Then, the cross-sectional area is progressively and smoothly increased to keep the velocity in the duct as low as possible and avoid pressure losses. However, this increase in area may conflict with the volume restrictions of the RPAS platform, so a compromise solution will be sought. A reduction in the section is made at the end of the route, prior to the entrance to the FC, to help reduce the effect of small local landslides and homogenize the flow, Fig. 12(a).

In addition, the placement of the proposed pitot-style air intake on the platform can be seen in Fig. 12(b).

Finally, based on the predimensioning carried out in the previous steps and the design limits (maximum contraction ratio, admissible distortion, and number of resistance divergence match), the established parameters can be optimized following practical design rules.

1) Estimating the pressure and distortion recovery produced by a certain contraction ratio.
2) Estimating the aerodynamic drag of the intake.
3) Selecting values to move to the wind tunnel test phase.

## VI. Results

Based on the electrical, mechanical and aerodynamics study carried out, the components selection and the final configuration of the hydrogen-powered fixed-wing RPAS are shown on Table VIII and Fig. 13.

Additionally, Fig. 14 shows the results obtained from simulation. The power demanded by the motor is stepped according to flight profile. During take-off phase, $0 < t \leq 0.6$ min, the brushless motor demands the maximum power (4 kW), which is provided by the battery, suffering a deep discharge. In the ascent phase, $0.6 < t \leq 2.4$ min, the demanded power by the motor is 2.7 kW and the battery is again solely responsible for powering the motor, reaching the end of its SOC (0%). During the cruise phase, $2.4 < t \leq 175.3$ min, the FC system will support the motor demand (800 W) and will recharge the battery (200 W available for this purpose). According to Table III, the total energy released by the battery during take-off and ascend is $4.35 \times 10^5$ J. Therefore, recharge time required by the battery is $4.35 \times 10^5$ J/200 W = 2178 seg (36.3 min); starting the recharging period at $t = 2.4$. Then, at $t = 38.7$ min (2.4 + 36.3 min), the battery is fully recharged (100% SOC), and the FC system only has to power the motor (800 W), $38.7 < t \leq 175.3$ min. Finally, descent phase ($175.3 < t \leq 180$ min) lasts 4.7 min to complete the 180-min flight autonomy with the hydrogen tank, and no power is required.

Additionally, hybridized hydrogen-based propulsion system is compared with previous gasoline-based engine and battery-based RPAS, Fig. 15.

As it can be observed, hybridized hydrogen-based propulsion system meets with flight requirements, guarantee 180-min autonomy and on-board battery recharge.

## VII. Conclusion

This article has presented an electrical design, mechanical sizing, and aerodynamics analysis to implement a low-emissions hydrogen-powered aircraft type fixed-wing RPAS.

The electrical design has allowed to select the equipment that meets with aircraft energy and power requirements. On the other hand, the mechanical sizing has been carried out to define the customized PEM FC as well as the calculation of the center of gravity of the aircraft. Finally, the aerodynamics findings permitted to know the air intakes' area to ensure the enough airflow inlet to oxygenate and cool the PEM FC, with a constant pressure and without significantly affecting the overall aerodynamics of the aerial platform.

It can be concluded that the proposed hydrogen-powered wing-fixed RPAS would provide the following advantages, in comparison with previous models.

### A. Increased Endurance

The hydrogen-batteries hybrid propulsion system allows for extended flight times and increased endurance (up to 200% regarding ICE RPAS version, and 100% with respect the battery-version RPAS), making it suitable for longer missions and surveillance tasks.

### B. Reduced Emissions

By using hydrogen as a clean energy source, the RPAS can significantly reduce its emissions (zero emissions), contributing to a greener and more sustainable operation.

### C. Lower Acoustic Footprint

The use of electric motor and a PEM FC results in quieter operations, minimizing noise pollution during flights. In this case, a reduction from 90 dB at 1 m to 65 dB at 1 m has been achieved.

TABLE IX
RPAS PERFORMANCE EVOLUTION

| | Gasoline RPAS | Battery RPAS | Hydrogen RPAS |
|---|---|---|---|
| Autonomy | 60 min | 90 min | 180 min |
| Emissions | 9 kg/kWh $CO_2$<br>3000 ppm CO<br>900 ppm $NO_X$ | 0 kg/kWh $CO_2$<br>0 ppm CO<br>0 ppm $NO_X$ | 0 kg/kWh $CO_2$<br>0 ppm CO<br><1 ppm $NO_X$ |
| Weight | 17.43 kg | 19.84 kg | 23.63 kg |
| Flight recharge | No | No | Yes |

### D. On-Flight Rechargeable

The passive control of the hydrogen-based electrical propulsion system, allows that the energy surplus from the PEM FC can be stored in the battery pack. This gives to hydrogen-based RPAS a special characteristic, that makes it unique: hydrogen-based RPAS is rechargeable during flight, reducing ground time, and increasing efficiency.

Table IX compares the performance of the hydrogen-powered RPAS designed in this article with the previous version of the same aircraft, ICE-version RPAS (internal combustion engine), and battery-version RPAS.

The aircraft used in this research does not have any type of aerial certification, as it was originally conceived as an aerial target. Thus, planning the certification of the aircraft after the fact could be an impossible task or, at the very least, very costly in time and money. In any case, this is not the objective of the research, but to demonstrate that it is possible to convert the aerial platform to run on hydrogen, thus achieving, among other features, much more autonomy. On the other hand, the state of research can be considered in TRL 3, i.e., design, sizing, and simulations from the electrical, mechanical, and aerodynamic point of view. This fills a gap in the previous scientific literature.

With the help and results obtained from this research work, it could be possible to undertake next phase: technology validation in lab (TRL 4) and under relevant operation conditions (TRL 5). Finally, to achieve a prototype that is a technological demonstrator (TRL 6). It is not intended to go further, because it is aware that it will only be possible to fly in controlled/segregated spaces. From here, the intention is to transfer the technology to other platforms where either type certification is available or where it is possible to participate in a specific certification program with the Spanish certification authority, the "Instituto Nacional de Técnica Aeroespacial" (INTA).

## REFERENCES


[1] P. J. Ansell, "Hydrogen-electric aircraft technologies and integration: Enabling an environmentally sustainable aviation future," *IEEE Electrific. Mag.*, vol. 10, no. 2, pp. 6–16, Jun. 2022, doi: 10.1109/MELE.2022.3165721.

[2] C. E. Jones et al., "A route to sustainable aviation: A roadmap for the realization of aircraft components with electrical and structural multifunctionality," *IEEE Trans. Transport. Electrific.*, vol. 7, no. 4, pp. 3032–3049, Dec. 2021, doi: 10.1109/TTE.2021.3078118.

[3] F. Bonfante, M. D. L. D. Vedova, P. Maggiore, and M. Battipede, "Evaluations on hydrogen fuel cells as a source of energy for specific operations category civil RPAS systems," *Int. J. Comput.*, vol. 2, pp. 1–6, Dec. 2017.

[4] J. Melgarejo and R. Furukawa, "Unmanned aerial vehicle design for pressure washing building facades in lima metropolitan area using hydrogen fuel cell," in *Proc. IEEE 29th Int. Conf. Electron., Electr. Eng. Comput. (INTERCON)*, Aug. 2022, pp. 1–4, doi: 10.1109/INTERCON55795.2022.9870088.

[5] D. Zeng, X. Guo, K. Guo, Z. Dong, and X. Yu, "Design and management of a hydrogen fuel cell powered quadrotor," in *Proc. Int. Conf. Unmanned Aircr. Syst. (ICUAS)*, Jun. 2023, pp. 644–651, doi: 10.1109/ICUAS57906.2023.10156500.

[6] N. Jenal, W. Kuntjoro, T. A. Ward, M. R. Aziz, and N. V. David, "A study on propeller performance of a fuel cell powered propulsion system," in *Proc. IEEE Int. Conf. Control Syst., Comput. Eng.*, Nov. 2012, pp. 557–561, doi: 10.1109/ICCSCE.2012.6487208.

[7] N. U. Hassan, B. Tunaboylu, and M. Yasin, "Development and technological steps for realization of AB-PEM fuel cell—A step towards clean & sustainable energy solutions," in *Proc. Int. Conf. Power Gener. Syst. Renew. Energy Technol. (PGSRET)*, Sep. 2018, pp. 1–6, doi: 10.1109/PGSRET.2018.8685934.

[8] F. I. Llerena, Á. F. Barranco, J. A. Bogeat, F. Segura, and J. M. Andújar, "Converting a fixed-wing internal combustion engine RPAS into an electric lithium-ion battery-driven RPAS," *Appl. Sci.*, vol. 10, no. 5, p. 1573, Feb. 2020, doi: 10.3390/app10051573.

[9] A. de las Heras, F. J. Vivas, F. Segura, and J. M. Andújar, "How the BoP configuration affects the performance in an air-cooled polymer electrolyte fuel cell. Keys to design the best configuration," *Int. J. Hydrogen Energy*, vol. 42, no. 17, pp. 12841–12855, Apr. 2017, doi: 10.1016/j.ijhydene.2016.11.051.

[10] E. Rivard, M. Trudeau, and K. Zaghib, "Hydrogen storage for mobility: A review," *Materials*, vol. 12, no. 12, p. 1973, Jun. 2019, doi: 10.3390/ma12121973.

[11] J. M. Andújar, F. Segura, J. Rey, and F. J. Vivas, "Batteries and hydrogen storage: Technical analysis and commercial revision to select the best option," *Energies*, vol. 15, no. 17, p. 6196, Aug. 2022, doi: 10.3390/en15176196.

[12] J. M. Andújar and F. Segura, "Fuel cells: History and updating. A walk along two centuries," *Renew. Sustain. Energy Rev.*, vol. 13, no. 9, pp. 2309–2322, Dec. 2009, doi: 10.1016/j.rser.2009.03.015.

[13] B. Barać, M. Krpan, and T. Capuder, "Modelling of PEM fuel cell for power system dynamic studies," *IEEE Trans. Power Syst.*, vol. 39, no. 2, pp. 3286–3298, Mar. 2024, doi: 10.1109/tpwrs.2023.3297741.

[14] V. Mehta and J. S. Cooper, "Review and analysis of PEM fuel cell design and manufacturing," *J. Power Sources*, vol. 114, no. 1, pp. 32–53, Feb. 2003, doi: 10.1016/s0378-7753(02)00542-6.

[15] R. Boddu, U. K. Marupakula, B. Summers, and P. Majumdar, "Development of bipolar plates with different flow channel configurations for fuel cells," *J. Power Sources*, vol. 189, no. 2, pp. 1083–1092, Apr. 2009, doi: 10.1016/j.jpowsour.2008.12.156.

[16] J. Scholta, F. Häussler, W. Zhang, L. Küppers, L. Jörissen, and W. Lehnert, "Development of a stack having an optimized flow field structure with low cross transport effects," *J. Power Sources*, vol. 155, no. 1, pp. 60–65, Apr. 2006, doi: 10.1016/j.jpowsour.2005.05.101.

[17] A. S. Andrés, J. L. M. García, and J. M. Ruiz, *Aerodinámica de las Tomas de Aire de las Aeronaves*. Madrid, Spain: Ibergaceta Publicaciones SL, 2012.

[18] *Mach Number. Role in Compressible Flows*, National Aeronautics and Space Administration, Washington, DC, USA, 2021.